Guiding Charge Injection in Schottky-barrier Transistors through the Spatial Fermi-level Gradients of Heterogeneous Bimetallic Systems

Min-Joong Kim[1], Woo-Seok Kim[1], Chang-Hyun Kim[2], Jin-Hyuk Kwon[3*], Min-Hoi Kim[1,3*]

[1]Department of Creative Convergence Engineering, Hanbat National University, Daejeon 34158, Republic of Korea.

[2]School of Electronic Engineering, Gachon University, Seongnam 13120, Republic of Korea.

[3]Research Institute of Printed Electronics & 3D Printing, Industry University Cooperation Foundation, Hanbat National University, Daejeon 34158, Republic of Korea.

***Corresponding authors:** Jin-Hyuk Kwon (Email: jhkwon@hanbat.ac.kr), Min-Hoi Kim (Email: mhkim8@hanbat.ac.kr)

The current density through a Schottky diode (J_S) is generally expressed as

$$J_S = A^* T^2 exp\left(-\frac{\Phi_B}{k_B T}\right)\left(\exp\left(\frac{qV}{nk_B T}\right) - 1\right) \tag{S1}$$

where A^* is the effective Richardson constant, T the temperature, Φ_B the Schottky barrier height, k_B the Boltzmann constant, q the elementary charge, V the voltage across the diode, and n the ideality factor. Based on Equation S1, the subthreshold drain current (I_D) of SB-TFTs, depending on the charge injection from the source, is expressed as

$$I_D = A_j A^* T^2 exp\left(-\frac{\Phi_b}{k_B T}\right)\left(1 - \exp\left(-\frac{qV_D}{nk_B T}\right)\right) \tag{S2}$$

where A_j is the Schottky contact area, Φ_b the Schottky barrier height at the source electrode/semiconductor interface, and V_D the drain voltage. The subthreshold I_D in a large-V_D region is nearly independent on V_D at ≈300 K (RT) as $V_D \gg nk_B T/q$. Thus, Equation S2 for a large-V_D region can be written as

$$I_D = A_j J_0 exp\left(-\frac{\Phi_b}{k_B T}\right) \tag{S3}$$

where $J_0 = A^* T^2$. Herein, the Φ_b is written as $\Phi_b = \Phi_{b,i} + \Delta\Phi_{b,GL}$ where $\Phi_{b,i}$ is the initial barrier height and $-\Delta\Phi_{b,GL}$ the V_G-induced barrier height lowering that reflects the image-force effect. Furthermore, the $\Delta\Phi_{b,GL}$ is given as $\Delta\Phi_{b,GL} = -\zeta q(V_G - V_{to})$ where ζ is the lowering sensitivity to V_G and V_{to} the turn-on voltage. Accordingly, we have the following equation for the subthreshold I_D of SB-TFTs:

$$I_D = A_j J_0 exp\left(-\frac{\Phi_{b,i}}{k_B T}\right) exp\left(-\frac{\Delta\Phi_{b,GL}}{k_B T}\right) \quad \text{S4}$$

where $\Delta\Phi_{b,GL} = -\zeta q\left(V_G - V_{to}\right)$.

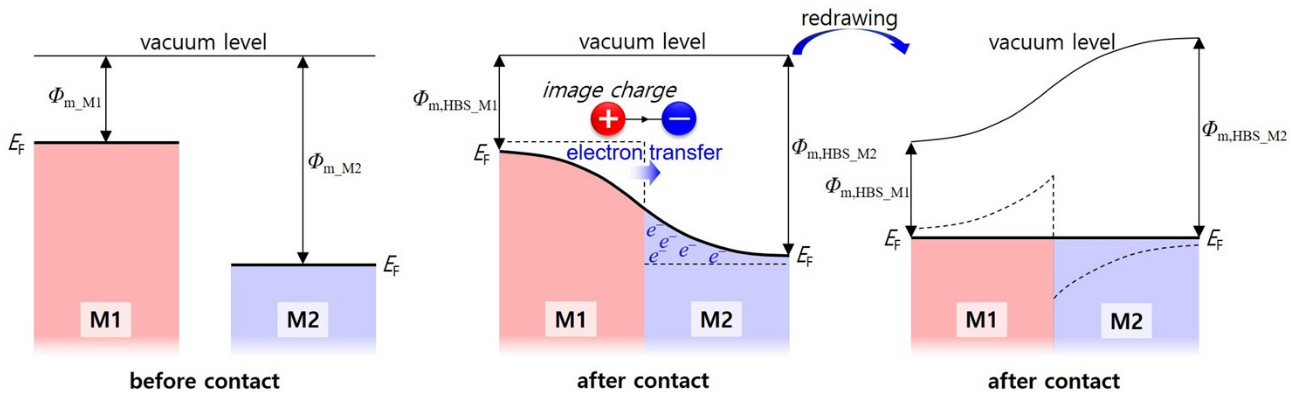

Figure S1. Schematic diagrams of the energy relations for the HBS-based thin film (i.e., with finite thickness).

Figure S1 shows the pre-contact and post-contact energy relations for a HBS composed of M1 and M2 layers with finite thickness. For the pre-contact energy relations, there exists a difference between the Φ_m of the M1 and M2 layers. When a junction is formed between M1 and M2 layers, i.e., either M1 or M2 layer approaches the other, the pre-contact Φ_m difference between them results in the electron transfer and the energy realignments. For the post-contact energy relations, the bending of the vacuum level represents the internal dipole and field formation resulting from the electron transfer and the corresponding charge distribution. HBS-based thin films with M1 and M2 can be formed using two different methods; one can be conducted by rendering either ready-made M1 or M2 layer adhere to the other through proper transfer techniques and the other by gradually growing each of M1 and M2 layers through consecutive thermal depositions. The former method is practically difficult due to the problems of low adhesion quality, severe mechanical damages, and etc. In our experiments, the M1 and M2 layers were formed with the latter method. In ideal situations, the condition of the post-contact energy relations at equilibrium should be identical regardless of the formation method. The present way of understanding the final energy relations is thus valid.

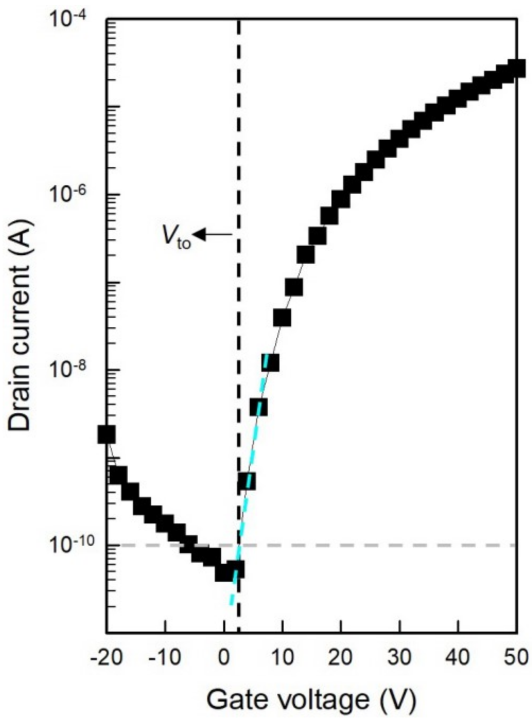

Figure S2. An example of the V_{to} extraction. The V_{to} extraction from the transfer characteristic curve of the IGZO SB-TFTs with the 80 nm-M1/10 nm-M2 SD electrodes.

As shown in **Figure S2**, we extracted all the V_{to} values by finding the V_G of the intersection between the I_{off} level of 1×10^{-10} A and the extrapolation line of the I_D data in the subthreshold region.

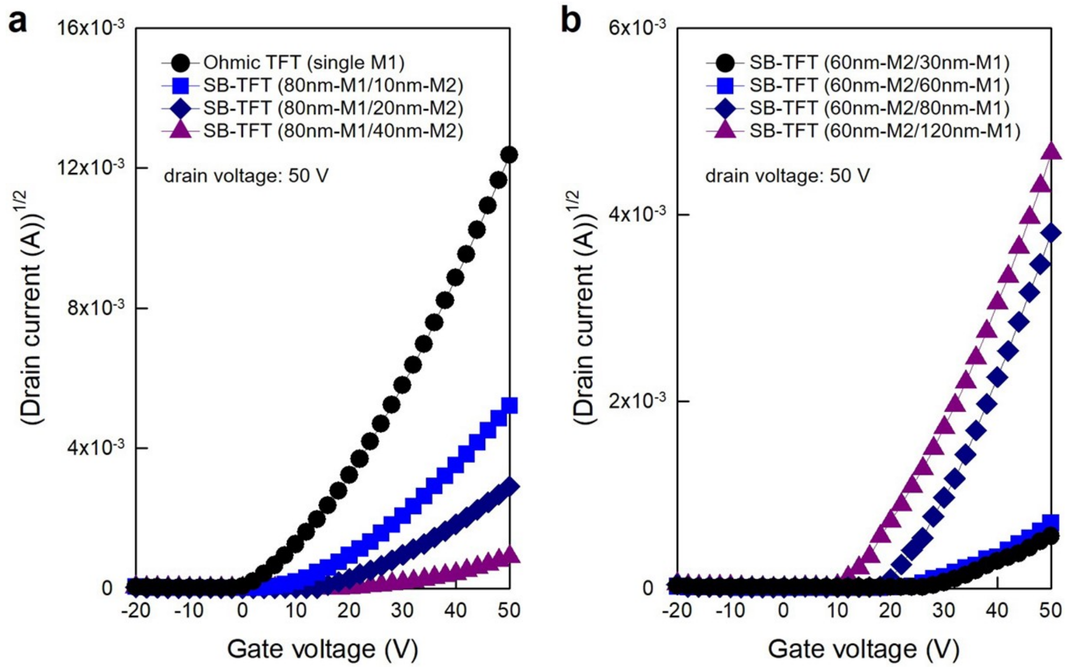

Figure S3. The $I_D^{1/2}$ *vs*. V_G plots of (**a**) the IGZO SB-TFTs with the M1/M2 SD electrodes and the IGZO ohmic TFT and (**b**) those with the M2/M1 SD electrodes.

The field-effect mobility (μ) in the saturation regime was extracted from the slope of the $I_D^{1/2}$ *vs*. V_G plots, based on the equation, $I_D = (W\mu C_i/(2L))(V_G - V_{th})^2$ where C_i is the gate-insulator capacitance and V_{th} the threshold voltage. For the M2/M1 case, the μ values of the 80 nm-M1/10 nm-M2, 80 nm-M1/20 nm-M2, and 80 nm-M1/40 nm-M2 cases were 0.78, 0.31, and 0.04 cm^2/Vs, respectively; the μ value for the ohmic TFT was 3.47 cm^2/Vs. For the M1/M2 case, the μ values of 60 nm-M2/30 nm-M1, 60 nm-M2/60 nm-M1, 60 nm-M2/80 nm-M1, and 60 nm-M2/120 nm-M1 cases were 0.69, 0.66, 0.03, and 0.02 cm^2/Vs, respectively. Moreover, the V_{th} was extracted through the linear extrapolation of the $I_D^{1/2}$ *vs*. V_G plot to zero I_D. For the M1/M2 case, the V_{th} values of the 80 nm-M1/10 nm-M2, 80 nm-M1/20 nm-M2, and 80 nm-M1/40 nm-M2 cases were 17.2, 20.9, and 27.2 V, respectively; the V_{th} value for the ohmic TFT was 11.5 V. For the M2/M1 SD case, For the M2/M1 case, the V_{th} values of the 60 nm-M2/30 nm-M1, 60 nm-M2/60 nm-M1, 60 nm-M2/80 nm-M1, and 60 nm-M2/120 nm-M1 cases were 28.1, 26.5, 23.9, and 18.9 V, respectively.

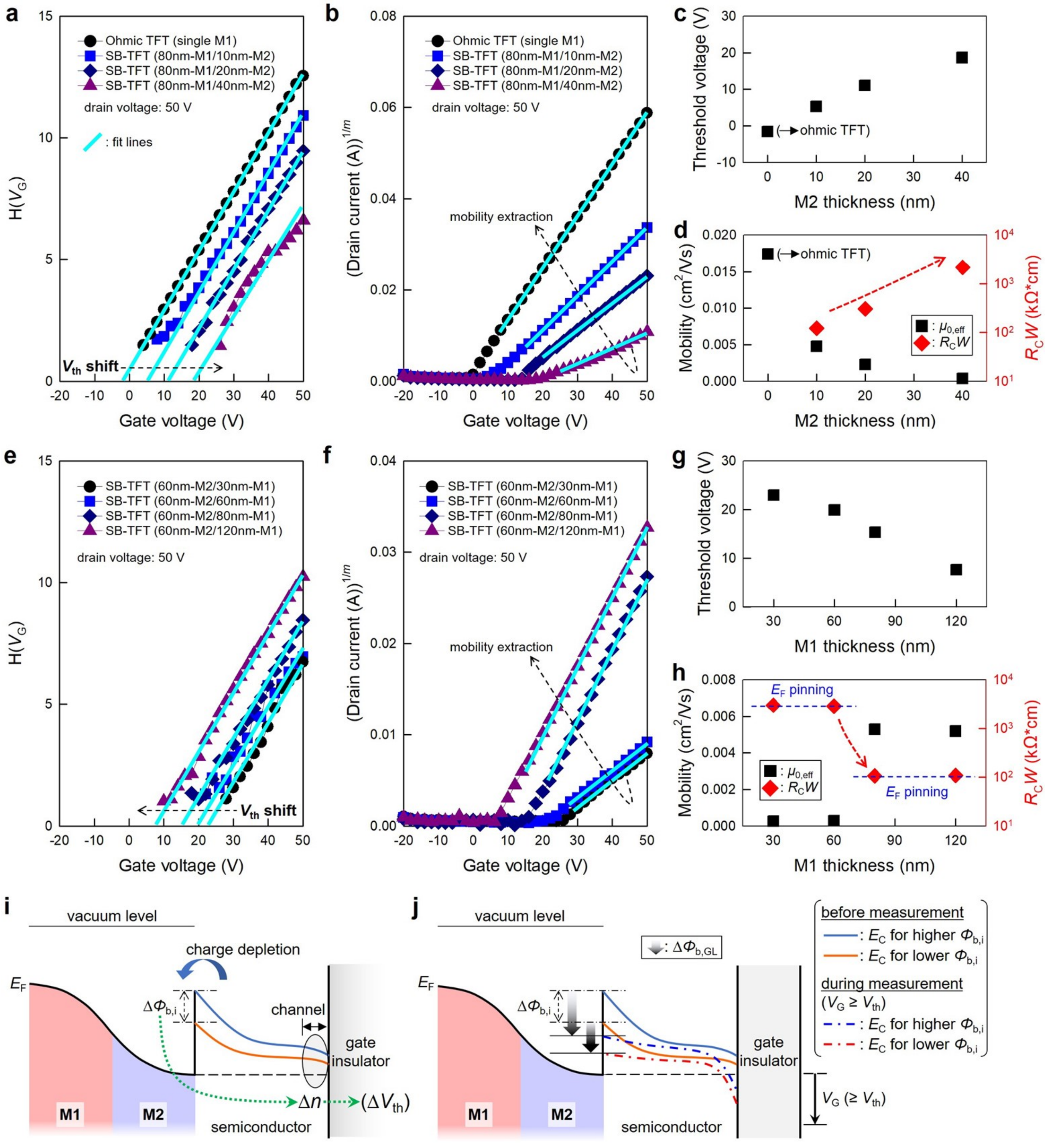

Figure S4. (**a**) The H(V_G) *vs*. V_G plots and (**b**) $I_D^{1/m}$ *vs*. V_G plots of the IGZO SB-TFTs with the M1/M2 SD electrodes and the IGZO ohmic TFT. The corresponding (**c**) V_{th}, (**d**) $\mu_{0,eff}$, and R_CW values in the M1/M2 case; the R_C was extracted at the V_G of 50 V. (**e**) The H(V_G) *vs*. V_G plots and (**f**) $I_D^{1/m}$ *vs*. V_G plots of the IGZO SB-TFTs with the M2/M1 SD electrodes. The corresponding (**g**) V_{th} and (**h**) $\mu_{0,eff}$, and R_CW values in the M1/M2 case; the R_C was extracted at the V_G of 50 V. Schematic diagrams of the energy relations (**i**) for a variation in the $\Phi_{b,i}$ accompanied by charge depletion in the semiconductor layer, and those for (**j**) a variation in the $\Phi_{b,i}$ followed by an increase in the R_C.

The transfer characteristics were further analyzed by using the H function (H(V_G)) [1,2], which is defined as $H(V_G) = \left(\int_0^{V_G} I_D dV_G\right) \Big/ I_D$. When the saturation I_D is given by $I_D = (WC_i\mu_{0,eff}/L)(V_G - V_{th})^m$ where C_i is the gate-insulator capacitance and $\mu_{0,eff}$ is the effective band mobility, the H(V_G) is equal to $(m+1)^{-1}(V_G - V_{th})$ by the definition. Accordingly, the V_{th} and m values of the devices were extracted from the linear slopes of the H(V_G) *vs.* V_G plots, as shown in **Figure S4**a and **S4**e. Firstly, for the M1/M2 case, the V_{th} values of the 80 nm-M1/10 nm-M2, 80 nm-M1/20 nm-M2, and 80 nm-M1/40 nm-M2 cases were 5.3, 11.1, and 18.7 V, respectively; the V_{th} value for the ohmic TFT was −1.6 V (**Figure S4**c). Compared to the ohmic TFT, the SB-TFTs had positively shifted V_{th}, which was attributed to the Schottky-barrier formation accompanied by the depletion of charges in the semiconductor layer. As the t_{M2} increased, the charge depletion was further intensified by the Schott-barrier formation with a larger $\Phi_{b,i}$, resulting in an increase in the V_{th} (see **Figure S4**i). For the M2/M1 SD case, the V_{th} values of the 60 nm-M2/30 nm-M1, 60 nm-M2/60 nm-M1, 60 nm-M2/80 nm-M1, and 60 nm-M2/120 nm-M1 cases were 23.0, 19.9, 15.3, and 7.6 V, respectively (**Figure S4**g). As the t_{M1} increased, the extent of charge depletion was reduced by the Schottky-barrier formation with a smaller $\Phi_{b,i}$, resulting in a decrease in the V_{th} (see **Figure S4**i).

Secondly, all the SB-TFTs and the ohmic TFT had similar m values of approximately 3.1 [3]. The $\mu_{0,eff}$ values of the devices were extracted from the linear slopes of the $I_D^{1/m}$ *vs.* V_G plots, as shown in **Figure S4**b and **S4**f. For the M1/M2 case, the $\mu_{0,eff}$ values of the 80 nm-M1/10 nm-M2, 80 nm-M1/20 nm-M2, and 80 nm-M1/40 nm-M2 cases were 0.0048, 0.0023, and 0.0004 cm^2/Vs, respectively; the $\mu_{0,eff}$ value for the ohmic TFT was 0.0174 cm^2/Vs (**Figure S54**d). Compared to the ohmic TFT, the SB-TFTs exhibited lower $\mu_{0,eff}$, which was attributed to the Schottky-barrier formation accompanied by an increase in the contact resistance (R_C). That is, the band mobility, μ_0 of the SB-TFTs was underestimated due to an increase in the R_C, which in turn implies the Schottky-barrier formation. As the t_{M1} increased, the R_C was increased by the Schottky-barrier formation with a larger $\Phi_{b,i}$, resulting in a reduction in the $\mu_{0,eff}$ (see **Figure S4**j). For a more specific discussion, the R_C dependence of $\mu_{0,eff}$ needs to be explored. The I_D is expressed as a function of R_C [4]:

$$I_D = \frac{(WC_i\mu/L)(V_G - V_{th,eff})V_D}{1 + R_C(WC_i\mu/L)(V_G - V_{th,eff})} \qquad \text{S5}$$

where μ is given by the power law, $\mu = \mu_0(V_G - V_{th,eff})^\gamma$, and $V_{th,eff}$ is the effective V_{th}. By substituting μ and V_D with $\mu = \mu_0(V_G - V_{th,eff})^\gamma$ and $V_{Dsat} = V_G - V_{th,eff}$ where V_{Dsat} is the saturation V_D, respectively, the I_D in the saturation region is written as:

$$I_D = \frac{(WC_i\mu_0/L)(V_G - V_{th,eff})^{\gamma+2}}{1 + R_C(WC_i\mu_0/L)(V_G - V_{th,eff})^{\gamma+1}} \qquad \text{S6}$$

Equation S6 can be rewritten as:

$$I_D = \frac{I_{D,0}}{1 + R_C g_{m,0}/(\gamma+2)} \qquad \text{S7}$$

where $I_{D,0}$, given by $I_{D,0} \equiv (WC_i\mu_0/L)(V_G - V_{th,eff})^{\gamma+2}$, represents the I_D for zero R_C and $g_{m,0}$, given by $g_{m,0} \equiv \partial I_{D,0}/\partial V_G$, represents the transconductance g_m for zero R_C. Based on Equation S7, the $\mu_{0,eff}$ is considered to be:

$$\mu_{0,eff} = \frac{\mu_0}{1 + R_C g_{m,0}/(\gamma+2)} \qquad \text{S8}$$

Note that Equation S8 reflects the R_C dependence of $\mu_{0,eff}$. As indicated by Equation S8, the μ_0 can be underestimated by the R_C. By rearranging Equation S8, the R_C is expressed as:

$$R_C = \frac{m}{g_{m,0}}\left(\frac{\mu_0}{\mu_{0,eff}} - 1\right) \qquad \text{S9}$$

where m is equal to $\gamma + 2$. Under the assumption that the μ_0 and $g_{m,0}$ in Equation S9 can be approximated by the $\mu_{0,eff}$ and g_m of the ohmic TFT, by inserting the m and $\mu_{0,eff}$ values of the SB TFTs into Equation S9, it is possible to infer the R_C values and relative variations thereof. Specifically, the width-normalized R_C (R_CW) values of the 80 nm-M1/10 nm-M2, 80 nm-M1/20 nm-M2, and 80 nm-M1/40 nm-M2 cases were 1.2×10^2, 3.0×10^2, and 2.2×10^3 kΩ*cm, respectively at the V_G of 50 V (**Figure S4**d). For the M2/M1 SD case, the $\mu_{0,eff}$ values of the 60 nm-M2/30 nm-M1 and 60 nm-M2/60 nm-M1 cases, 60 nm-M2/80 nm-M1, and 60 nm-M2/120 nm-M1 cases were 0.00026, 0.00028, 0.00529, and 0.00519 cm^2/Vs, respectively (**Figure S4**h). As the t_{M1} increased, a step-like increase in the $\mu_{0,eff}$ was observed (**Figure S4**h). An aluminum oxide (AlO_x) layer was possibly formed between the SD/semiconductor interface, hence creating a high density of interfacial traps, i.e., AlO_x-associated energy states. A reduction in the R_C led to the increase in the $\mu_{0,eff}$, while the step-like variation was presumably due to E_F pinning induced by the interfacial traps [5]. The R_CW values of the 60 nm-M2/30 nm-M1 and 60 nm-M2/60 nm-M1 cases, 60 nm-M2/80 nm-M1, and 60 nm-M2/120 nm-M1 cases were 3.0×10^3, 2.9×10^3, 1.1×10^2, and 1.1×10^2 kΩ*cm, respectively at the V_G of 50 V (**Figure S4**h). Large and directional variations in the R_CW values were observed in both the M1/M2 and M2/M1 cases, indicating the Schottky-barrier formation.

References

[1] A. Ortiz-Conde, A. Cerdeira, M. Estrada, F. J. G. Sanchez and R. Quintero, *Solid-State Electron.*, 2001, **45**, 663-667.

[2] A. Cerdeira, M. Estrada, R. Garcia, A. Ortiz-Conde and F. J. G. Sanchez, *Solid-State Electron.*, 2001, **45**, 1077-1080.

[3] S. Lee, A. Nathan, Y. Ye, Y. Guo and J. Robertson, *Sci. Rep.*, 2015, **5**, 13467.

[4] S. Jung, J. W. Jin, V. Mosser, Y. Bonnassieux and G. Horowitz, *IEEE Trans. Electron Devices*, 2019, **66**, 4894-4900.

[5] T. Gallet, D. Grabowski, T. Kirchartz and A. Redinger, *Nanoscale*, 2019, **11**, 16828-16836.

.

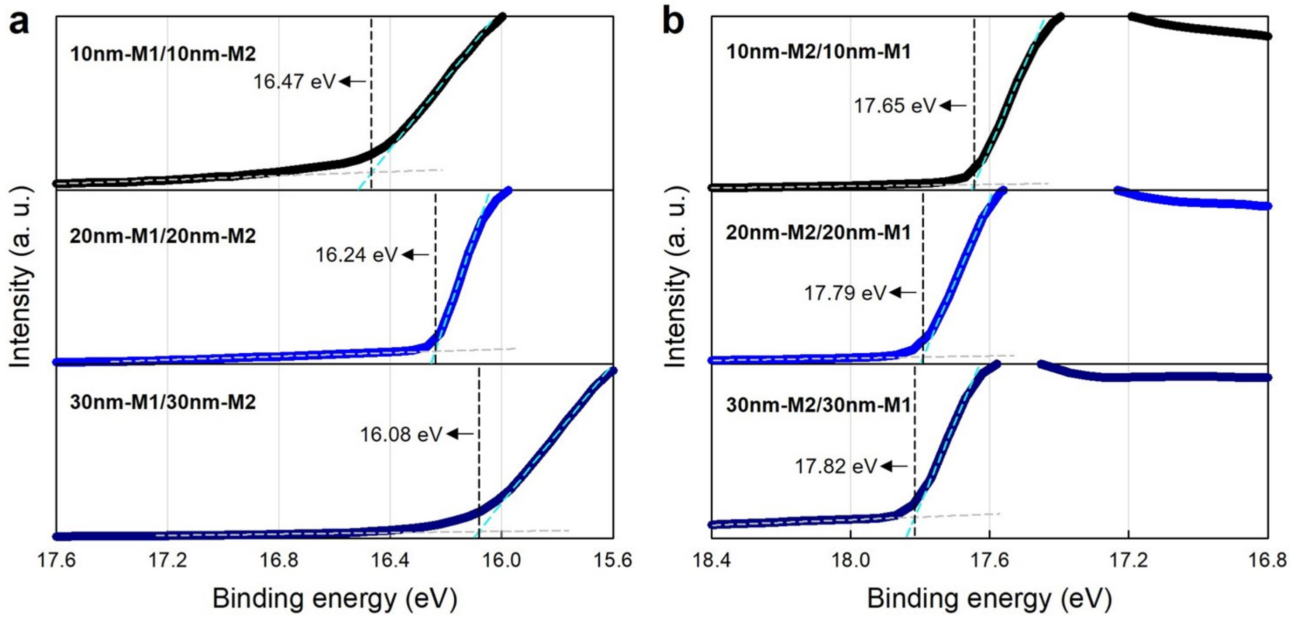

Figure S5. (**a**) The UPS spectra in the secondary-electron cut-off regions (with the corresponding fit lines and E_{co} values) in the M1/M2 case (i.e., 10 nm-M1/10 nm-M2, 20 nm-M1/20 nm-M2, and 30 nm-M1/30 nm-M2), and (**b**) those in the M2/M1 case (i.e., 10 nm-M2/10 nm-M1, 20 nm-M2/20 nm-M1, and 30 nm-M2/30 nm-M1).

For the M1/M2 case, the cut-off energy (E_{co}) values of the 10 nm-M1/10 nm-M2, 20 nm-M1/20 nm-M2, and 30 nm-M1/30 nm-M2 thin films were 16.47, 16.24, and 16.08 eV, respectively. The corresponding $\Phi_{m,HBS}$ values of the 10 nm-M1/10 nm-M2, 20 nm-M1/20 nm-M2, and 30 nm-M1/30 nm-M2 thin films were 4.75, 4.98, and 5.14 eV, respectively. For the M2/M1 case, the E_{co} values of the 10 nm-M2/10 nm-M1, 20 nm-M2/20 nm-M1, and 30 nm-M2/30 nm-M1 thin films were 17.65, 17.79, 17.82 eV, respectively. The corresponding $\Phi_{m,HBS}$ values of the 10 nm-M2/10 nm-M1, 20 nm-M2/20 nm-M1, and 30 nm-M2/30 nm-M1 thin films were 3.57 3.43, and 3.40 eV, respectively.

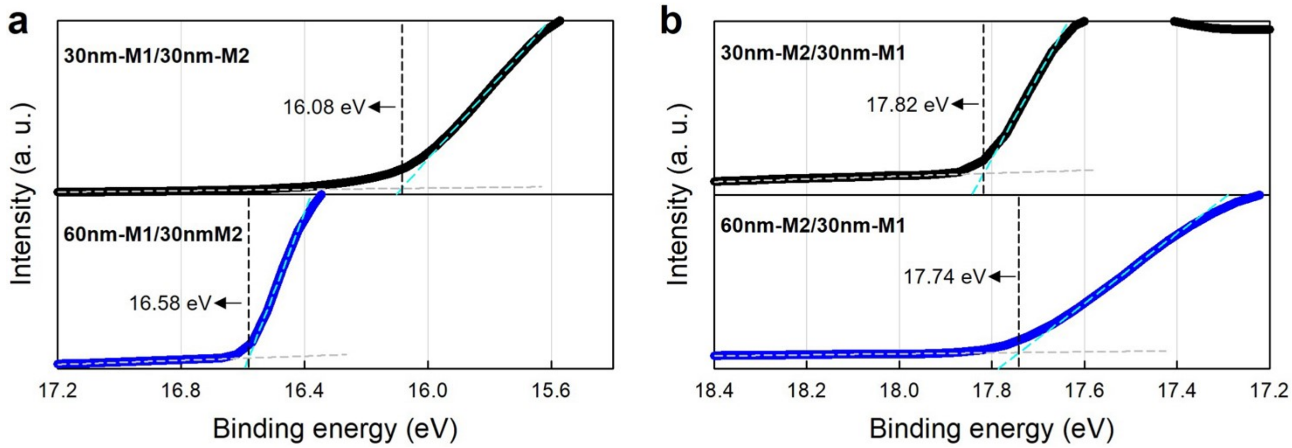

Figure S6. (**a**) The UPS spectra in the secondary-electron cut-off regions (with the corresponding fit lines and E_{co} values) in the M1/M2 case (i.e., 30 nm-M1/30 nm-M2 and 60 nm-M1/30 nm-M2), and (**b**) those in the M2/M1 case (i.e., 30 nm-M2/30 nm-M1 and 60 nm-M2/30 nm-M1).

For the M1/M2 case, the cut-off energy (E_{co}) values of the 30 nm-M1/30 nm-M2 and 60 nm-M1/30 nm-M2 thin films were 16.08 and 16.58 eV, respectively. The corresponding $\Phi_{m,HBS}$ values of the 30 nm-M1/30 nm-M2 and 60 nm-M1/30 nm-M2 thin films were 5.14 and 4.64 eV, respectively. For the M2/M1 case, the E_{co} values of the 30 nm-M2/30 nm-M1 and 60 nm-M2/30 nm-M1 thin films were 17.82 and 17.74 eV, respectively. The corresponding $\Phi_{m,HBS}$ values of the 30 nm-M2/30 nm-M1 and 60 nm-M2/30 nm-M1 thin films were 3.40 and 3.48 eV, respectively.

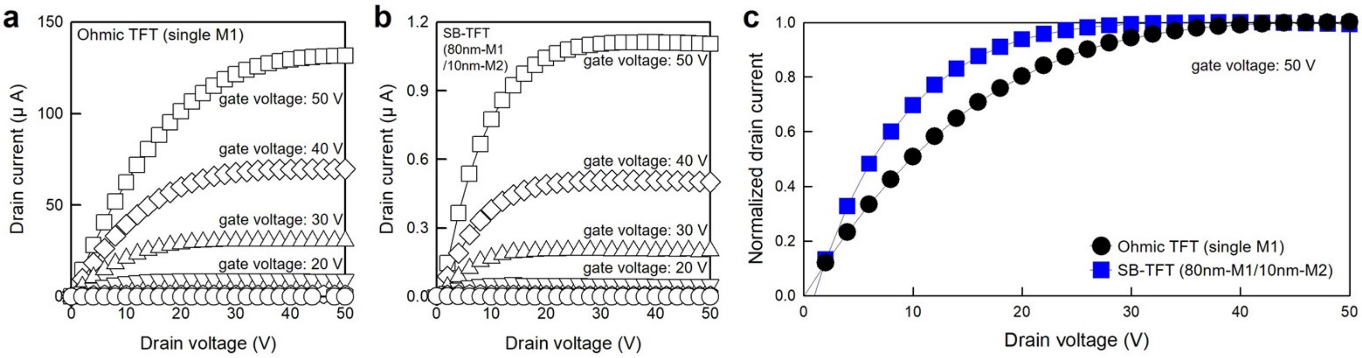

Figure S7. The output characteristic curves of (**a**) the ohmic TFT and (**b**) the SB-TFT with the 80 nm-M1/10 nm-M2 SD electrodes, respectively. (**c**) The normalized I_D *vs*. V_D plots of the IGZO SB-TFT and the IGZO ohmic TFT.

The I_D saturation behaviors in the output characteristics of the ohmic TFT and SB-TFTs were compared to further examine the influences of the Schottky-barrier formation. **Figure S7**c shows the normalized I_D *vs*. V_D plots of the SB-TFT and the ohmic TFT. The normalization was carried out by dividing the I_D data by the maximum value for each curve. The SB-TFT exhibited the saturation of I_D at lower V_D than the ohmic TFT and the I_D curve of the SB-TFT was flatter than that of the ohmic TFT. The I_D saturation at lower V_D of the SB-TFT is presumably due to charge depletion in the semiconductor layer. Due to complex causality and correlations between diverse intertwined factors including the charge depletion, depletion capacitance, contact resistance, curve shift, and mobility, it is difficult to identify the role and contribution of each factor for the saturation behaviour. Further research is needed to thoroughly investigate the operating mechanism of SB-TFTs.

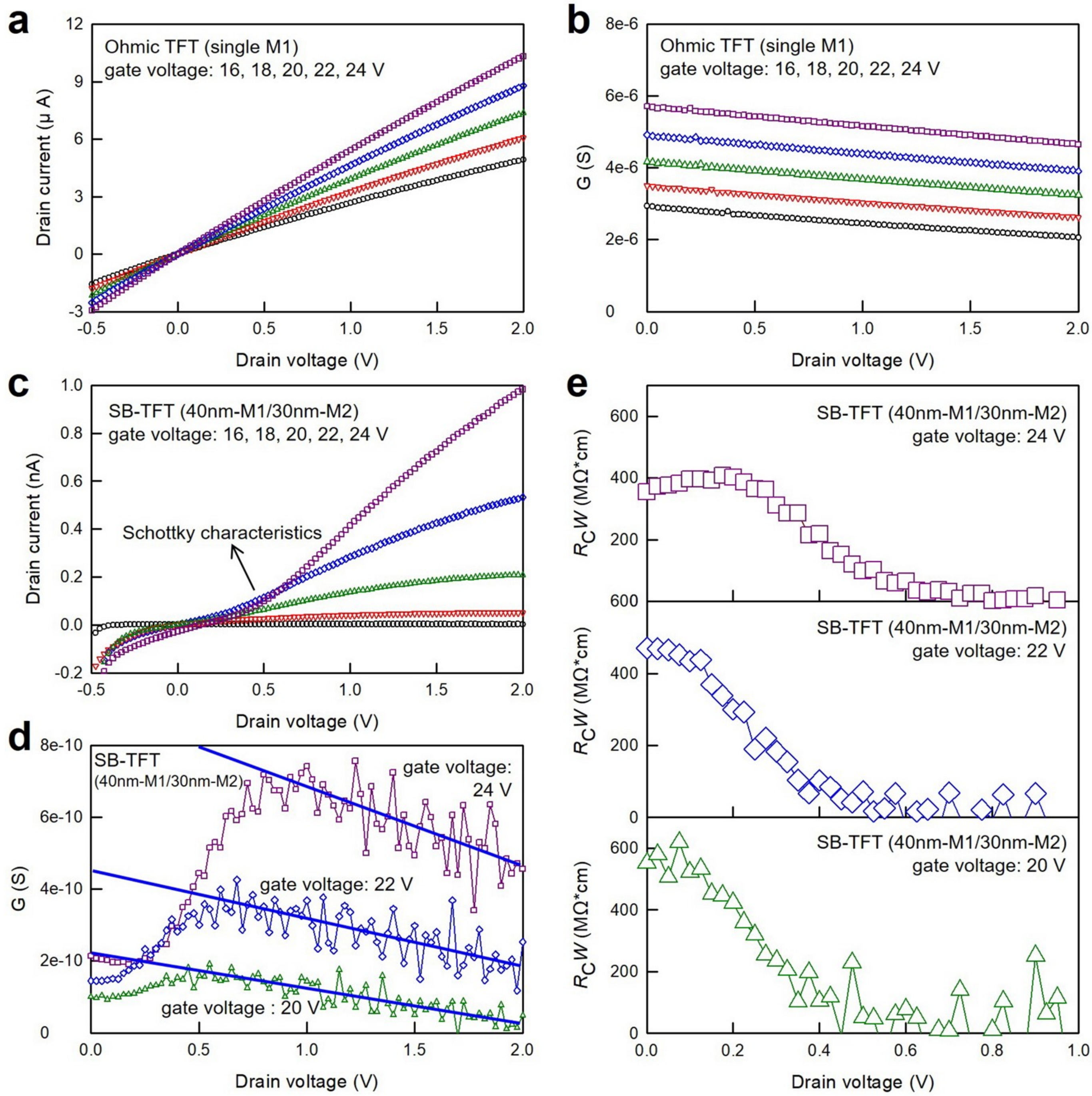

Figure S8. (**a**) The output characteristic curves and (**b**) output conductance of the ohmic TFT in a small-V_D region. (**c-e**): The G-function analyses. (**c**) The output characteristic curves, (**d**) output conductance with linear fit lines, and (**e**) extracted R_C of the SB-TFT with the 40 nm-M1/30 nm-M2 SD electrodes in a small-V_D region.

The output characteristics of the ohmic TFT exhibited good linearity in a small-V_D region (**Figure S8**a). **Figure S8**b shows the corresponding output conductance, which is given by $G = \partial I_D/\partial V_D$. By contrast, those of the

SB-TFT with the 40 nm-M1/30 nm-M2 SD electrodes exhibited non-linearity (i.e., S-shape) in a small-V_D region (**Figure S8**c). The output characteristic curves were measured by sweeping V_D from −0.5 V to 2 V in 25 mV increments. We performed G-function analyses for the output characteristics of the SB-TFT. **Figure S8**d shows the corresponding output conductance, which exhibits an abrupt increase followed by a linear decrease. **Figure S8**e shows the extracted R_C values of the SB-TFT for different V_Gs. The R_C of the SB-TFT exhibited a dependence on V_G, indicating the V_G-induced lowering of the injection barrier (**Figure S8**e).

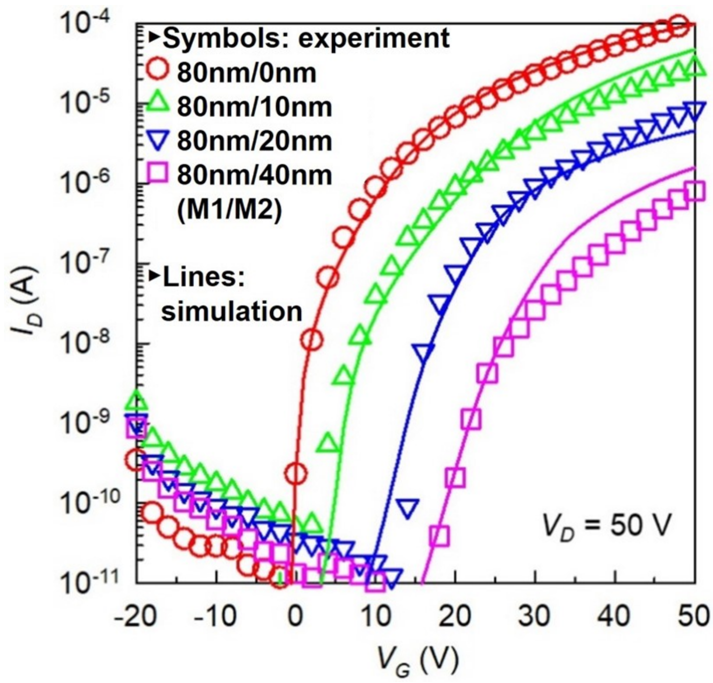

Figure S9. Comparison between the experimental and simulated transfer characteristics of the IGZO TFTs with the ohmic and M1/M2 SD contacts.

For physical investigation, a two-dimensional (2D) finite-element solver was used (ATLAS, Silvaco). This simulator solves the coupled Poisson's and drift-diffusion equations over the 2D mesh to calculate both the electrostatic distributions and the terminal characteristics. The simulation was performed with a single metallic layer for the SD electrodes, with different Φ_ms. We changed the Φ_b in simulation by fixing the electron affinity of IGZO and by modifying the SD Φ_m. The data from the ohmic TFT (single-M1 case) were first analyzed to obtain the basic fitting parameters. An exponential density of states for the acceptor-like traps was introduced to further improve the fitting quality. For the TFTs with the HBS-based SD electrodes, the same Φ_bs directly measured by UPS were inserted as a simulation input parameter. Then, the trap parameters were re-adjusted to reproduce the effects of possible interfacial and material origins, which enabled an optimum fit of each transfer curve with the comparable level of V_{to} shift. **Figure S9** shows an excellent agreement between the measured and simulated data. The simulation procedure confirmed that the Φ_m modulation by the addition of M2 and the $\Delta\Phi_b$ thereof is a major factor of the V_{to} shift.

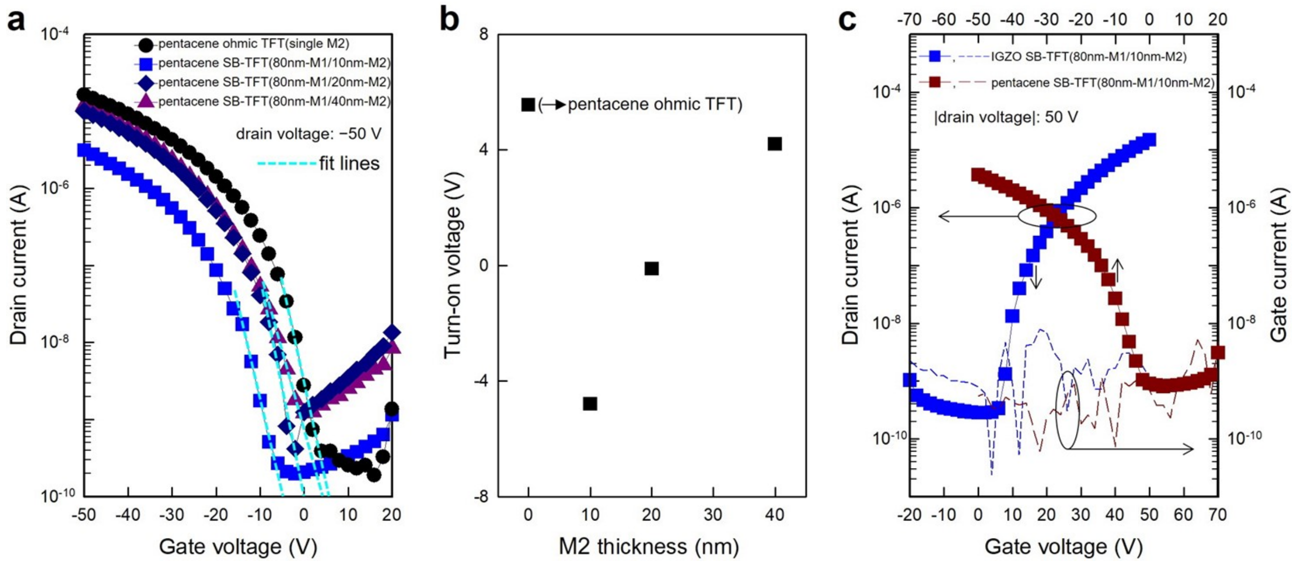

Figure S10. (**a**) The transfer characteristic curves of the pentacene SB-TFTs with the M1/M2 SD electrodes and the pentacene ohmic TFT, (**b**) the corresponding V_{to} values, and (**c**) the transfer characteristic curves (plotted together with the gate current) of the IGZO and pentacene SB-TFTs with the 80 nm-M1/10 nm-M2 SD electrodes.

The electrical characteristics of the pentacene SB-TFTs with the HBS-based SD electrodes were explored as well. **Figure S10**a shows the transfer characteristic curves of the pentacene SB-TFTs with the M1/M2 SD electrodes (i.e., 80 nm-M1/10 nm-M2, 80 nm-M1/20 nm-M2, and 80 nm-M1/40 nm-M2) and the pentacene ohmic TFT with bare 60 nm-M2 SD electrodes. For the pentacene SB TFTs, the V_{to} values of the 80 nm-M1/10 nm-M2, 80 nm-M1/20 nm-M2, and 80 nm-M1/40 nm-M2 conditions were, −4.80, −0.11, and 4.21, respectively; that of the pentacene ohmic TFT was 5.56 V (**Figure S10**b). As the M2 thickness increased from 10 nm to 40 nm, the V_{to} of the pentacene SB TFT increased and approached that of the pentacene ohmic TFT (**Figure S10**b). The increase in the V_{to} was attributed to the increase in the Φ_{m,HBS_M2} followed by a reduction in the $\Phi_{b,i}$. The pentacene SB-TFT with the 80 nm-M1/10 nm-M2 SD electrodes exhibited a clear off-state feature and an electrical performance comparable with the IGZO SB-TFT with 80 nm-M1/10 nm-M2 SD electrodes (**Figure S10**c).

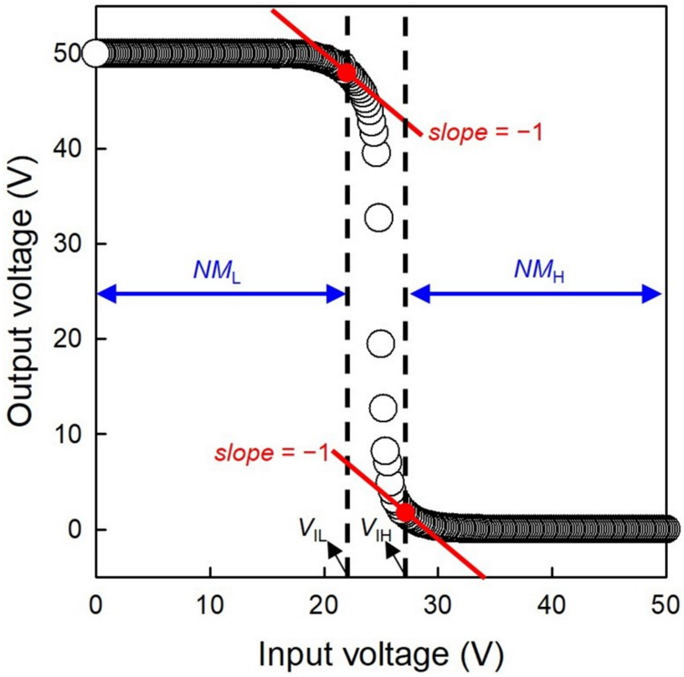

Figure S11. The details for the noise-margin calculation from the voltage transfer characteristic of the complementary inverter.

Figure S11 shows the details for calculating the noise-margin of the complementary inverter. The high- and low-state noise margin values (NM_H and NM_L, respectively) were calculated from $NM_H = V_{OH} - V_{IH}$ and $NM_L = V_{IL} - V_{OL}$, respectively, where $V_{IH} = 26.7\ V$, $V_{OH} = 50.0\ V$, $V_{IL} = 22.8\ V$, and $V_{OL} = 0.0\ V$ (**Figure S11**). Accordingly, the NM_H and NM_L values were 23.3 and 22.8 V, respectively.